AUT Journal of Electrical Engineering

AUT J. Elec. Eng., 58(2) (2026) 247-262
DOI: 10.22060/eej.2026.24345.5687

High Gain Modified Reboost-Luo Converter with Optimized PI Controller for Effectual Integration of PV in Grid System

Kosuri Sravani*, Challa Leela Kumari, Puttagunta Manisha, Rayudu Sowmya Deepika, Yadla Manoj

Department of Electrical and Electronics Engineering, Godavari Institute of Engineering and Technology (A), Rajahmundry, India.

ABSTRACT: In recent years, Renewable Energy Sources (RES) have gained substantial importance in the global energy generation landscape, offering numerous environmental and economic benefits. This paper presents a highly efficient Photovoltaic (PV) grid-tied system utilizing a novel High-Gain Modified Re-Boost Luo (HG-MRBL) converter, designed to optimize energy generation. For attaining optimal energy production from solar panels, Maximum Power Point Tracking (MPPT) is employed using Jellyfish Search Algorithm, by an Adaptive Neuro-Fuzzy Inference System (JSA-ANFIS). An HG-MRBL converter processes the PV system's output to raise Direct Current (DC) voltage to the necessary levels for grid interaction. A three-phase Voltage Source Inverter (VSI) applied for converting this DC supply into AC. To minimize harmonics and guarantee seamless grid integration, the VSI is connected to an LC filter. Proportional Integral (PI) controller utilized for controlling injection of both active and reactive power into grid to manage flow of power. The system's efficiency is validated using MATLAB simulation, revealing the highest converter efficiency of 94.31%, which surpasses the performance of state-of-the-art approaches.

Review History:

Received:
Revised:
Accepted:
Available Online:

Keywords:

Renewable Energy Sources
Photovoltaic System
High-Gain Modified Re-Boost Luo Converter
Jellyfish Search Algorithm
ANFIS MPPT
PI Controller

1- Introduction

Global warming and population expansion are causing a rapid depletion of conventional energy supplies, prompting an increasing number of people to turn toward using green energy. Therefore, integrating various RES into the existing power grid provides users with better options for enhancing overall reliability of power system. This is due to the integration of RES with their improved adaptability in smart grid operations [1], [2]. Since power generation is stochastic, high-level integration of RE with a utility grid raises concerns regarding both systems' stability and dependability. A PV system converts the solar energy into DC power. Output of solar array is affected by temperature, cloud cover, and atmospheric durability [3], [4].

PV typically produces low-voltage DC, which needs to be converted to high voltage using DC-DC converters. High PV output voltage has been achieved by numerous traditional DC-DC converters, such as Boost, Buck, and Cuk converters. If an output power is required to be greater than the input, Boost converters [5] are found to be more advantageous. On the contrary, the Buck converters [6] have a high efficiency and reduce the input voltage, which makes it appropriate for applications that require a lower output voltage. Cuk converters [7] are widely known for their ability to provide a stable output while inverting the voltage polarity. However, in comparison to boost and buck converters, they tend to be less effective and more complicated. When integrating PV systems into grid applications, each converter type has its own set of benefits and drawbacks. The primary drawback is that low voltage gains are often present in these converters, which are problematic when dealing with large input and output voltage differentials. Modified buck and Cuk converters [8] offer an appealing alternative to deal with these problems. By adding characteristics that boost performance and efficiency under particular conditions, modified buck converters outperform the conventional buck design. Comparably, modified Cuk converters offer a flexible solution with improved performance than traditional buck-boost designs because of their capacity to deliver both step-up and step-down voltage conversion while inverting polarity. But these modified converters have some challenges, such as increased circuit complexity and potential cost implications. Henceforth, the design of a novel converter is essential to overcome the limitations of existing converter topologies.

Modified converters have evolved as a solution to these problems, but they come with additional drawbacks such as potential cost implications and higher circuit complexity. Traditional MPPT techniques, including Hill Climbing

*Corresponding author's email: emandisravani8@gmail.com

(HC) [9], Perturb and Observe (P&O) [10], and Incremental Conductance (IncCond) [11] frequently utilized to lessen the shortcomings. Despite the complexity of modified converters, these strategies efficiently increase energy extraction from PV systems by continuously modifying the operating point, improving total system efficiency. P&O fluctuates around the maximum power point, HC is slower and less effective when partially shaded, and IncCond, while correct, are computationally expensive and complex. Intelligent MPPT control systems have replaced the limitations of conventional approaches. Artificial Neural Networks (ANN) [12], Fuzzy Logic [13], and ANFIS [14] are some of the often utilized techniques. ANN has the benefit of being able to learn intricate correlations and adjust to changing circumstances, but it is additionally data-intensive and prone to overfitting. Fuzzy Logic offers easy control and strong performance in uncertain conditions, but in highly dynamic scenarios, it may not be as accurate. ANFIS, which combines the advantages of Fuzzy Logic with ANN, enables increased efficiency and adaptability but frequently necessitates large computational resources. Particle Swarm Optimization (PSO) [15], Grey Wolf Optimization (GWO), Whale, firefly, and other intelligent optimization techniques to overcome the limitations of these methodologies, which enhance the efficiency of MPPT strategies in solar systems. However, PSO has drawbacks, including its limited capacity to adjust to rapidly changing environmental conditions, sensitivity to parameter values, and potential problems with local minima. Due to these limitations, this research work introduces a novel JSA-ANFIS MPPT with robustness and adaptability through its hybrid approach. Thereby, improved supply is fed to the grid system for supplying energy to various applications.

1- 1- Contributions

The following contributions add value to the proposed work.

The work proposed here introduces a number of significant innovations that, combined, advance the performance and dependability of PV systems as the underlying platform for testing next-generation power conversion and tracking mechanisms. This architecture is formulated to support dynamic environmental conditions without compromising operating stability, thus facilitating practical assessment of the improvements proposed here. The HG-MRBL converter presents a highly enhanced power conversion efficiency and voltage regulation of the PV system. Through the use of hybrid gain and multi-resonant bridge-link topologies, the converter reduces the switching loss and enhances voltage stability with different load conditions. This contribution is highly significant for the purpose of providing steady energy supply and maximizing the overall solar energy system performance. Execution of JSA-ANFIS MPPT algorithm inspired by adaptive nature of Jellyfish Search Algorithm exhibits faster tracking speed and accuracy in maximizing power harvesting from solar panels. By blending the exploratory nature of JSA with the learning adaptability of ANFIS, the new MPPT approach exhibits high sensitivity to irradiance dynamics and thus maximum energy harvesting efficiency under varied operating conditions.

2- Proposed System Description

This work is designed with the architecture and development of three-phase grid-connected solar PV system. The design combines an optimized PI controller with a high-efficiency power conversion path, as shown in Fig. 1, for stable energy supply and successful grid synchronization. The work emphasizes grid-connected mode and power quality improvements through sophisticated control and filtering techniques.

Solar panels are an initial component of the proposed system, which captures sunlight and transforms it into DC. Following that, the generated DC enters through the HG-MRBL converter, which effectively raises the voltage to satisfy grid integration specifications. The system utilizes a JSA-ANFIS for MPPT to maximize energy harvesting from the solar panels. This innovative system reacts to changes in temperature and sun irradiation to continuously optimize the solar panels' operating conditions and ensure maximum efficiency. The resulting DC link supply is sent to three-phase VSI for active AC conversion. Pulse Width Modulation (PWM) generator then processes the VSI output, regulating the inverter's switching to change the output voltage and frequency in accordance with grid requirements. The system reacts to load variations more efficiently by using a PI controller to reduce errors between the desired and actual output. By promoting the efficient use of renewable resources, the system design contributes to a sustainable energy future while also improving energy stability and efficiency.

3- Proposed System Modeling

3- 1- Solar PV Module

To assure energy generation, solar PV panels convert solar radiation into DC electricity. Several solar cells arranged on a surface and linked in series or parallel to increase power output comprise a solar cell module, sometimes referred to as a PV module. Fig. 2 illustrates equivalent circuit of single diode solar cell.

PV cell consists of current source I_g which denotes the generated photocurrent due to solar irradiance, a diode d for modeling the p-n junction characteristics, a parallel resistance R_p that accounts for leakage current, and series resistance R_S which represents losses in cell's contacts and interconnections. To determine the PV current, Equation 1 is utilized as follows,

$$I_{PV} = I_g - I_d - I_p \tag{1}$$

Where the diode current is represented as I_d and I_p is current that passes through parallel resistance R_p .By using Ohm's law,

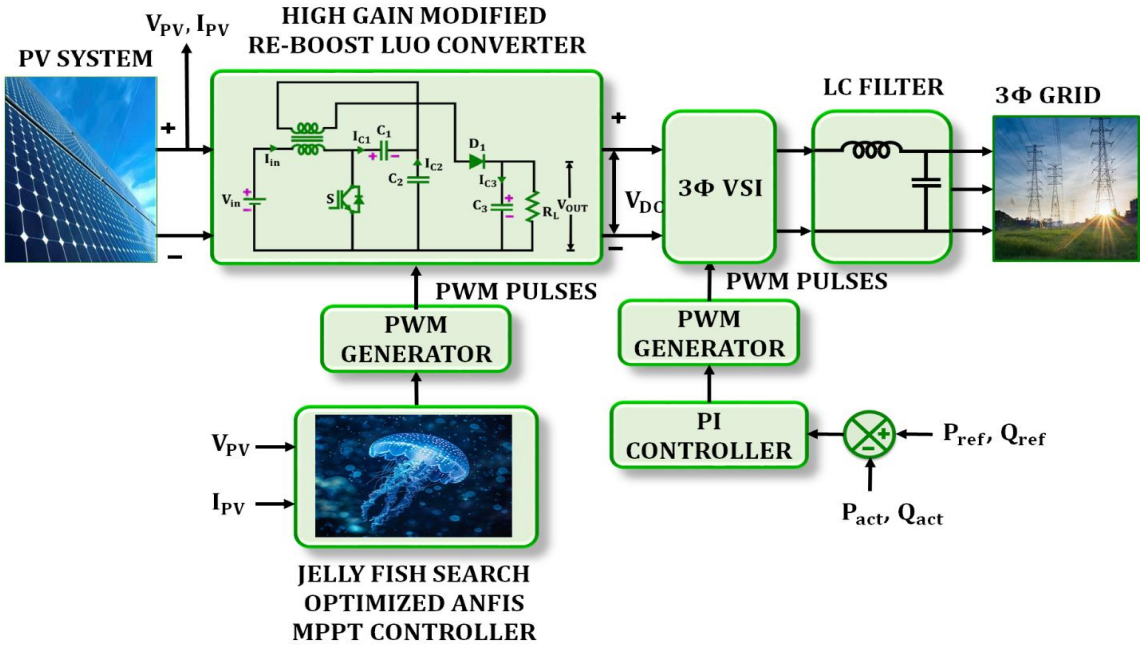

Fig. 1. Proposed Work Block Diagram.

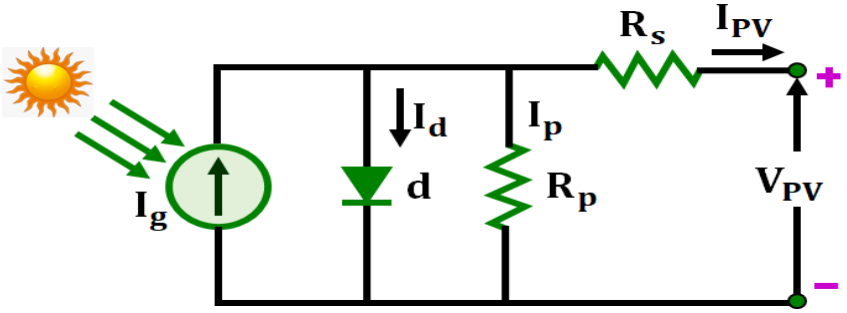

Fig. 2. Equivalent circuit of a PV cell.

$$I_P V = I_g - I_s\left(e^{((V_P V + I_P V R_s)/nVt)} - 1\right) - \left((V_P V + I_P V R_s)\right)/R_p \quad (2)$$

Here, I_s is diode's reverse saturation current, V_t is thermal voltage, and V_{PV} is output voltage of PV cell and its behaviour under various temperature and irradiance circumstances is modelled by Equation 2. Because of climate change, the voltage attained from PV system is low. This is improved by using proposed HG-MRBL, which is explained below.

3- 2- Modeling and Operation of Proposed Converter

Proposed HG-MRBL converter addresses the drawbacks of traditional DC–DC converters that often involve multiple components, resulting in increased losses and control complexity. The HG-MRBL employs a single active switch (S), one diode (D), three capacitors (C_1, C_2, C_3), and a coupled inductor L, greatly simplifying the topology and minimizing conduction losses. Its high voltage transformation ratio capability with small components makes it an ideal choice for grid system and RES applications where compactness, reliability, and efficiency are essential.Fig.3 shows equivalent structure of proposed HG-MRBL converter.

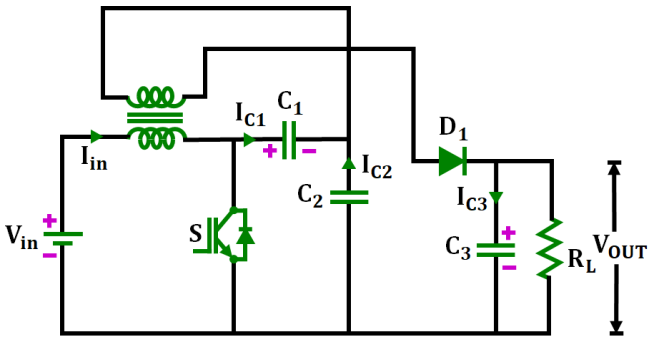

Fig. 3. Structure of HG-MRBL converter.

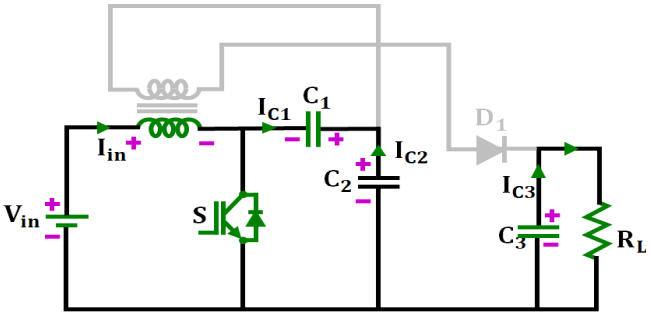

Fig. 4. Proposed HG-MRBL converter Mode 1 of operation.

Transformer Magnetic Design Details

The coupled inductor L is designed such that the desired step-up ratio is achieved without core saturation.

Turns Ratio Selection: The turn's ratio $n = N_2 / N_1$ is selected according to the desired output voltage V_0:

$$V_0 = n\frac{(2-\alpha)}{(1-\alpha)}V_{in} \tag{3}$$

Where, α is the duty cycle.

Core Selection: A ferrite core with large saturation flux density (B_{sat}) and small core loss is used to reduce the magnetizing current and keep the efficiency high.

Magnetizing Inductance: Structured such that the ripple of the magnetizing current stays between 20–30% of the average current.

$$L = \frac{V_{in} \cdot \alpha T_s}{\Delta I_L} \tag{4}$$

Where, T_s is the switching time and ΔI_L is peak-to-peak ripple current.

Mode 1:

Mode 1, as shown in Fig. 4, has S in the ON position, which allows current to pass through the inductor L. In this phase, the primary inductor is magnetized, capacitor C_1 charges, and capacitor C_2 discharges. Reverse current flow is prevented by the diode's operation in the OFF position. Furthermore, capacitor C_3 releases the energy it has stored, powering the load. This mode efficiently enables energy transmission and storage, preparing the converter for its following operation.

$$V_{L(ON)} = V_{in} \tag{5}$$

Mode 2:

Mode 2 is shown in Fig. 5, where S is turned OFF, releasing stored power in primary inductor. By passing over transformer, this energy causes a voltage that supports the charging of capacitor C_2 and the discharging of capacitor C_1. This mode ensures continuous power delivery by causing the diode to become forward-biased, which permits current to flow to the load. To stabilize the load supply, capacitor C_3 is essential since it keeps the output voltage constant as it releases energy. This mode maximizes efficiency and performance while improving the converter's capacity to increase voltage.

$$V_{L(ON)} = V_{in} = \frac{V_{C1}}{n} \tag{6}$$

For steady state operation:

$$V_{L(ON)} \cdot \alpha T_s + V_{L(ON)} \cdot (1-\alpha) T_s = 0 \tag{7}$$

Substituting,

$$V_{in}\alpha T_s + \left(V_{in} - \frac{V_{c1}}{n}\right)(1-\alpha)T_s = 0 \tag{8}$$

Solving for V_{c1},

$$V_{c1} = n\frac{2-\propto}{1-\propto}V_{in} \tag{9}$$

The proposed converter's output potential difference is as follows:

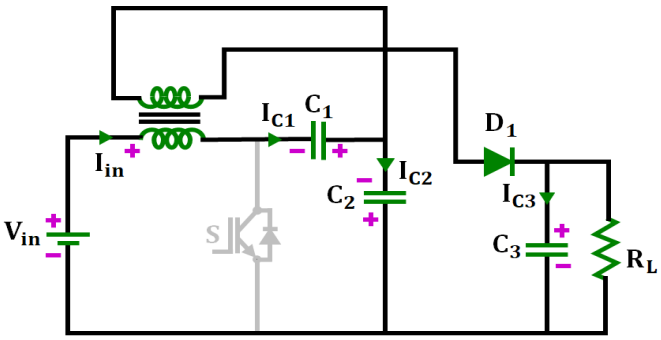

Fig. 5. Proposed HG-MRBL converter Mode 2 of operation.

$$V_o = V_{c1} = \mathrm{n}\left(\frac{(2-\propto)}{(1-\propto)}\right)V_{in} \tag{10}$$

Where the duty cycle is mentioned as a . From Equation (4),

$$Output\ Gain\ G = \frac{(V_o)}{V_{in}} = \mathrm{n}\left(\frac{(2-\propto)}{(1-\propto)}\right) \tag{11}$$

When both primary and secondary windings of transformer are connected in cascade configuration, transformer operates as an inductor. Leakage inductance of coupled inductor causes short voltage spikes during the turn-off transient of the switch, and it slightly raises voltage stress on switch and diode. This parasitic component also creates a small decrease in the effective voltage gain since some of the stored energy is lost during the transient phase. In order to ensure accuracy, the leakage inductance is modeled in the simulation as a series element with an approximate value of 1–3% of the magnetizing inductance, as this faithfully reproduced its effects on switching waveforms and current ripple without compromising the steady-state gain performance. The total current flowing through both the capacitor and the inductor is referred to as the input current. The rate of electron flow, or input current I_{in} , is determined by

$$I_{in} = I_L + I_{C1} \tag{12}$$

$$I_0 = \frac{V_O}{R} \tag{13}$$

$$\triangle V_O = \frac{V_O(1-\propto)}{fc2R} \tag{14}$$

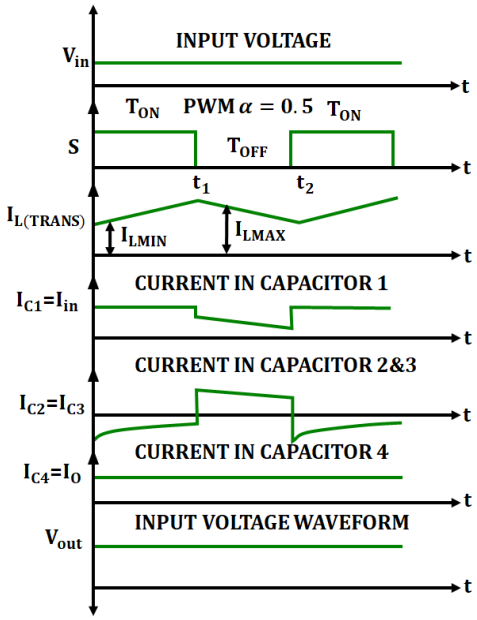

Fig. 6. Switching Waveform of HG-MRBL.

$$V_{in} = V_O\left(\frac{1-\propto}{2-\propto}\right) \tag{15}$$

$$I_{in} = \frac{V_{in}}{R} = \frac{V_0}{R}\left(\frac{1-\propto}{2-\propto}\right) \tag{16}$$

$$\frac{V_{in}}{I_{in}} = \left(\frac{1-\propto}{2-\propto}\right)^2 \cdot \frac{V_0}{V_0/R} \tag{17}$$

The proposed HG-MRBL converter realizes partial Zero-Current Switching (ZCS) at turn-ON as the switching current is almost zero when switching on. At turn-OFF, the demagnetizing current of the coupled inductor reduces the slope of the current and thus the turn-off loss and voltage stress. This soft-switching action is responsible for the high overall efficiency (94.31%) demonstrated in simulation results.

$$\frac{V_{in}}{I_{in}} = \left(\frac{1-\propto}{2-\propto}\right)^2 .R \tag{18}$$

Proposed converter switching waveform is presented in Fig. 6. It is simple Luo converter containing of three diodes and three capacitors. With a transformer acting as an inductor, a significant output gain is possible. The input voltage in the proposed converter causes a change in the capacitance C_1 .

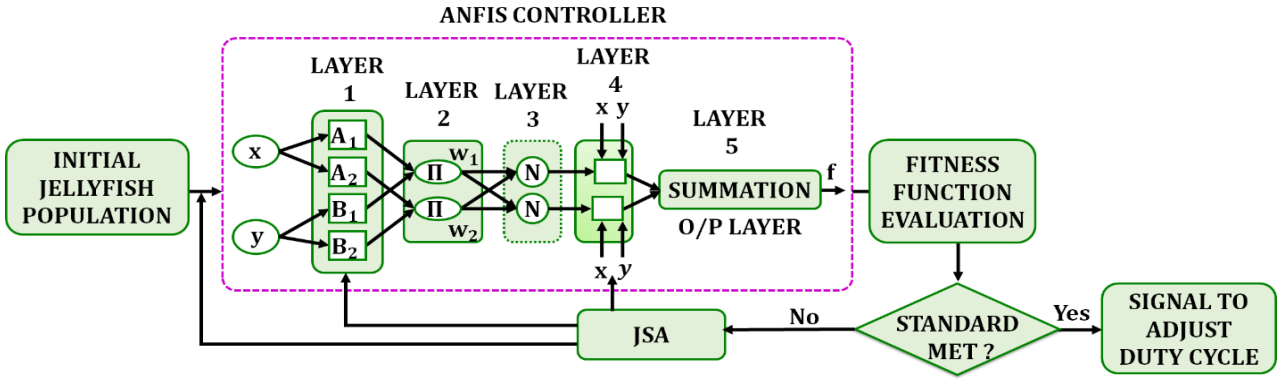

Fig. 7. Architecture of optimized ANFIS.

The following describes the ripple current of the transformer's primary winding:

$$\triangle I_L = \frac{V_{in}.\propto T}{L} \tag{19}$$

$$V_{C1} = V_0 \tag{20}$$

$$V_{C2} = \left(\frac{2-\propto}{1-\propto}\right) V_{in} \tag{21}$$

The potential difference at the proposed converter's output is,

$$V_0 = \frac{N_2}{N_1}\left(\frac{2-\propto}{1-\propto}\right) V_{in} \tag{22}$$

Secondary winding's number of turns is denoted by N_2, whereas primary winding's number is denoted by N_1. Number of spins and duty cycle of the converter determine the potential difference at the converter's output. Fig. 5 represents the timing waveform.

3- 3- Proposed Hybrid ANFIS- Jelly Fish Optimized MPPT Controller

An ANFIS controller is an effective tool for MPPT in a variety of applications because it efficiently combines the advantages of Fuzzy Logic Controller (FLC) with neural networks. The ability to deal with uncertainties and nonlinearities frequently found in RES by its distinctive architecture. An ANFIS-based controller ensures optimal energy extraction from solar panels by having a quick convergence speed and improved tracking accuracy when compared to other intelligent MPPT approaches. By integrating an ANFIS controller, the power conversion system becomes more efficient by effectively generating the ideal duty ratio for a proposed converter. The controller precisely controls its membership parameters by using fuzzy membership functions. Through this procedure, linguistic variables are converted into numerical values, which improves the precision of the FLC operation.

The optimized ANFIS structure is displayed in Fig. 7. Two sample fuzzy rules are implemented as follows

Rule 1:

If x is A_1 and y is B_1

Then,

$$f_1 = \omega_1.(a.x + b.y + c) \tag{23}$$

where,

A_1 and B_1 are the membership functions for both x and y the normalized strength from layer 3 is denoted as ω_1 and a, b, c are the parameters for the linear function in layer 4.

Rule 2:

If x is A_2 and y is B_2

Then

$$f_2 = \omega_2.(p.x + q.y + r) \tag{24}$$

Here p, q, r are the parameters for the linear function in layer 4.

In the proposed work, ANFIS controller performance is optimized significantly by the JSA-ANFIS MPPT technique. This is made possible by a special hybrid algorithm that combines ANFIS's adaptive capabilities with dynamic exploration techniques modelled after jellyfish effects. Using a combination of back-propagation and least squares

algorithms, this method precisely optimizes and fine-tunes the membership functions to guarantee that the parameters are appropriately set for best performance.

To increase tracking performance of ANFIS controller, its parameters get tuned with the aid of JSA, a metaheuristic influenced by jellyfish foraging in ocean currents. By using a temporal control system with a constant C_O and a time-dependent function C_t, the JS algorithm controls the movements of jellyfish by alternating between swarming activities and following ocean currents. Food gathering efficiency is influenced by jellyfish locations and accompanying goal functions, and the system replicates the process of searching for food by producing random values between 0 and 1.

The JSA is predominantly beneficial for MPPT as it dynamically alternates between exploration (following ocean currents) and exploitation (swarming movements), enabling both global search and fine local convergence. This adaptive balance prevents premature convergence and agrees algorithm to quickly track true MPP even under rapid irradiance and temperature fluctuations. Unlike PSO, which is prone to stagnation around local optima, JSA's type-A and type-B motion strategies help the search agents escape local minima efficiently, leading to faster convergence and higher tracking accuracy.

The objective function and population size are first defined in jellyfish swarming, which then iterates through the system a predetermined number of times. The flowchart for the JSA-ANFIS MPPT controller is shown in Fig. 8. An initial control time of the series is set to 1, and initial positions of the jellyfish are obtained by determining their distance from a given point using a chaotic map. To find out if there are ocean currents, the control time is then compared to 0.5. If the jellyfish is following the current, the ocean current is used to determine its new location. A jellyfish traveling inside the swarm, on the other hand, uses both passive and aggressive motion characteristics to find its new place. After that, the algorithm's output is examined, and the JSA is utilized in PV system optimization to determine MPPT of the system.

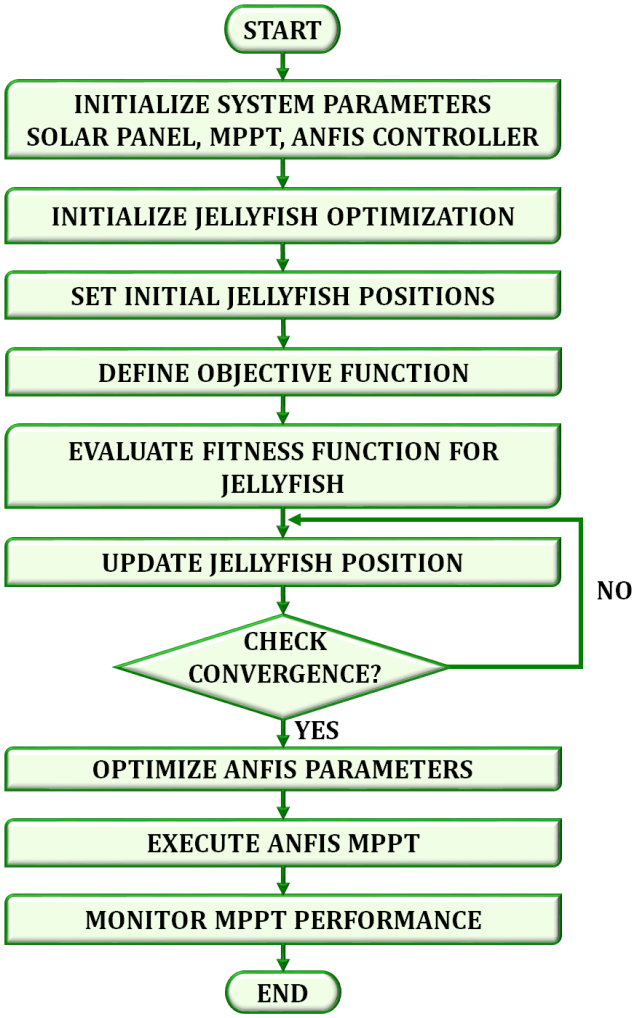

Fig. 8. Flow chart for JSA-ANFIS MPPT.

Calculation of the ocean current:

$$X_i(t+1) = X_i(t) + rand(0,1) * \left(X^* - \beta * rand(0,1) * \mu\right) \tag{25}$$

Distribution coefficient is denoted by β, where μ is average location of all jellyfish and $\beta > 0$. Because they offer a wealth of nutrients, jellyfish are drawn to water currents. As per equation (25), the aggregate of all the paths that a jellyfish takes in the ocean to reach its current ideal location is used to depict movement of an ocean current. The following provides each jellyfish's updated location:

$$X_i(t+1) = X_i(t) + \gamma^* rand(0,1) * (U_b - L_b) \tag{26}$$

The majority of the jellyfish in the swarm display type A movement patterns when it initially emerge. More type B movement behaviours start to appear over time. A jellyfish is considered to be in active motion when it moves within its own area. Equation (26) gives each jellyfish's most recent position based on this movement. Every jellyfish's location is updated as a result of this operation, where the mobility coefficient is $\gamma > 0$. A jellyfish's direction of motion and its most updated location:

$$|Direction| = \begin{cases} X_j(t) - X_j(t) \text{ if } f(X_i) \geq f(X_i) \\ X_i(t) - X_j(t) \text{ if } f(X_i) < f(X_i) \end{cases} \tag{27}$$

Every jellyfish in the swarm obtains food by moving in the most effective direction to this procedure. A successful local search is achieved by using equation (27) to characterize the jellyfish's movement and updated location based on the best

direction. The control mechanism of time:

$$c(t)=\left|1-\frac{t}{Max\ iteration}\right|\times\left(2\times rand\left(0,1\right)-1\right) \tag{28}$$

To determine the kind of motion taking place at a specific moment, the time control function $c(t)$ and the constant c_o are utilized. Type A and type B swarm movements are managed by this temporal control system, which also manages jellyfish's migration in route of an ocean current. Maximum number of jellyfish in a search area:

$$X_{i,d}^{'}=\begin{cases}X_{i,d}-U_{b,d}+L_{b(d)}, & if\ upper\ bound\ exceeded\\ X_{i,d}-L_{b,d}+U_{b(d)}, & if\ lower\ bound\ exceeded\end{cases} \tag{29}$$

Location of i^{th} jellyfish in the dimension d^{th} is denoted by $X_{i,d}$, and updated location following the application of boundary constraints is denoted by $X_{i,d}$. Equation (29) specifies some boundary requirements pertaining to the jellyfish's ocean current to define the area's limits. The electrical components of the PV system serve as the algorithm's devices, and the algorithm mimics the movements of jellyfish in the search space. The following is an expression of the objective function for applying the jellyfish algorithm to improve output power

$$f(x)=\frac{P_{out}}{V_{PV}} \tag{30}$$

Where $f(x)$ is fitness function, x is vector of decision factors (duty ratio and other pertinent variables), P_{out} is PV system's output power, and V_{PV} is PV panel's voltage. The duty ratio, which is determined by dividing the converter's on-time by its switching period, is used to regulate power flow between PV panel and DC-DC converter.

3- 4- Grid Synchronization

Phase-Locked Loop (PLL) is a widely used synchronization method for identifying phase angle of grid voltages, providing reliable performance during the presence of noise or harmonics. It works in dq -frame by converting the sensed three-phase grid voltage e_{abc} into DC components by Park transformation.

$$\begin{bmatrix}e_d\\ e_q\end{bmatrix}=\begin{bmatrix}\cos(\theta) & \cos\left(\theta-\frac{2\pi}{3}\right) & \cos\left(\theta+\frac{2\pi}{3}\right)\\ -\sin(\theta) & -\sin\left(\theta-\frac{2\pi}{3}\right) & -\sin\left(\theta+\frac{2\pi}{3}\right)\end{bmatrix}\begin{bmatrix}e_a\\ e_b\\ e_c\end{bmatrix} \tag{31}$$

By setting desired direct-axis voltage component e_d^* to zero, the PLL operate s as a phase detector.

$$error=e_d^*-e_d \tag{32}$$

A PI controller adjusts the phase error to zero, acting as a loop filter.

$$u(t)=K_p e_{error}+K_i\int e_{error}dt \tag{33}$$

Structure of PLL for grid synchronization is presented in Fig. 9. The resultant signal, combined with nominal grid frequency ω_{ff} represents grid frequency.

$$\omega=\omega_{ff}+ut(t) \tag{34}$$

The output passes through Voltage Controlled Oscillator (VCO), typically an integrator, for producing synchronized phase angle (θ).

$$\theta=\int\omega dt \tag{35}$$

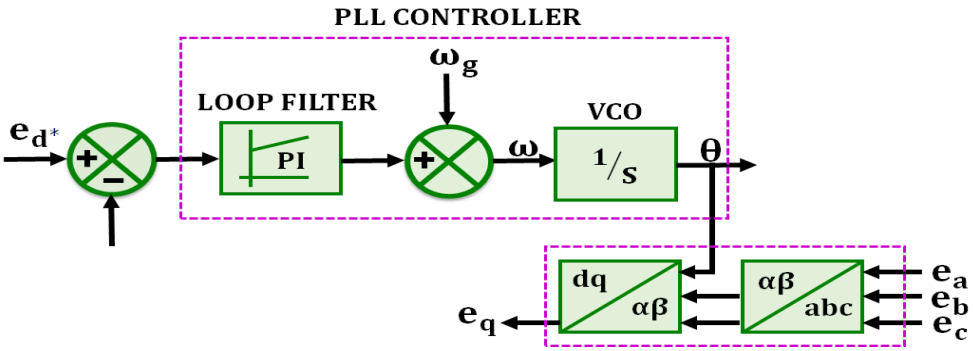

Fig. 9. Grid Synchronization structure of PLL.

Table 1. Parameter Specification.

Parameter	Rating
Solar PV System	
Power	10kW
Short circuit current	8.33A
Short circuit voltage	12V
Open circuit voltage	22.6V
High-Gain Modified Re-Boost Luo (HG-MRBL)	
C_1, C_1	$870\mu F$
Output Capacitor, C_0	$2200\mu F$
Coupled inductor	$1.1mH$
Switching frequency	10kHz

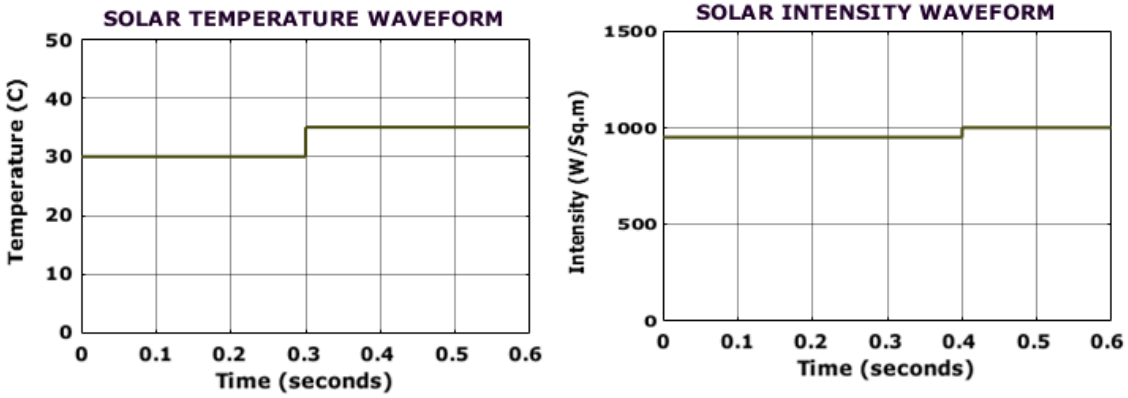

Fig. 10. Temperature and Intensity waveform of solar panel.

These equations form the basis of the PLL system, enabling precise synchronization of inverter's output with the grid's voltage, phase, frequency, and amplitude.

4- Results and Discussion

In results section, findings specify that proposed PV grid-tied system with HG-MRBL converter exhibits notable improvements in several key performance. Table 1 provides detailed specifications of PV system and converter used in simulation, further illustrating the system's design and operational parameters.

Under Varying Temperature and varying intensity

Fig.10 shows PV panel temperature and intensity waveforms under varying temperature and varying intensity condition. Temperature stabilizes at 35°C in waveform shown, indicating a steady and consistent thermal environment for the PV system. This constant temperature is essential for preserving peak performance since temperature variations might reduce PV modules' efficiency. Furthermore, at 1000 W/m², the usual irradiance level for the peak sunlight, the solar irradiation stabilizes.

Fig.11 signifies PV panel input voltage and current waveforms under both temperature and intensity varying case. PV system's voltage is continuously kept at 80V, ensuring that the power conversion process operates within the desired voltage range. Furthermore, after a short interval of 0.51 seconds, the current stabilizes at 88A with only slight variations. The slight current variations that persist after stabilization are insignificant, demonstrating that the control procedures managed the behaviour of the system.

Fig.12. presents the proposed HG-MRBL characteristic waveform under varying environmental conditions. Voltage rapidly stabilizes at 830V, while the current settles at 8A, both achieving steady-state within 0.1s. The minimal fluctuations highlight the converter's stability and efficiency in providing high voltage gain. These results validate its reliability for grid-tied renewable energy applications.

Fig.13 displays the input and output power waveforms of proposed converter under changing temperature and intensity scenario. The input power initially peaks at 3.1×10^4 W

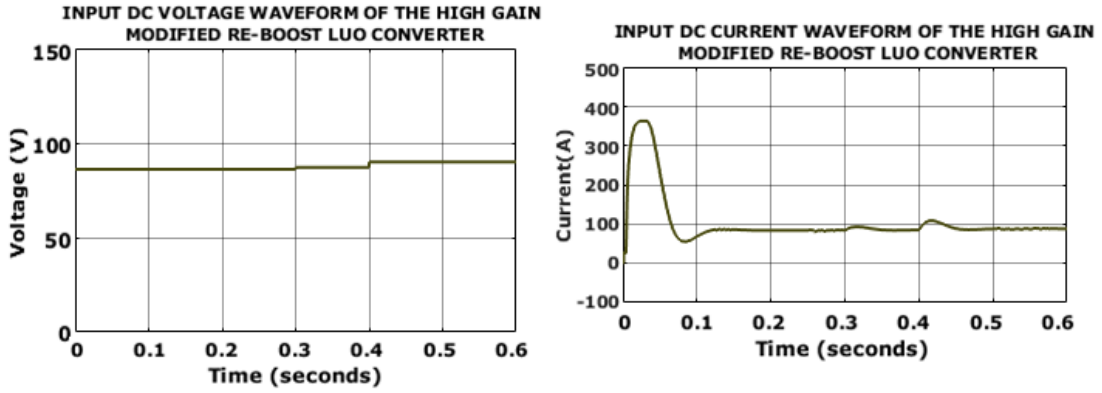

Fig. 11. Voltage and Current waveform of solar panel.

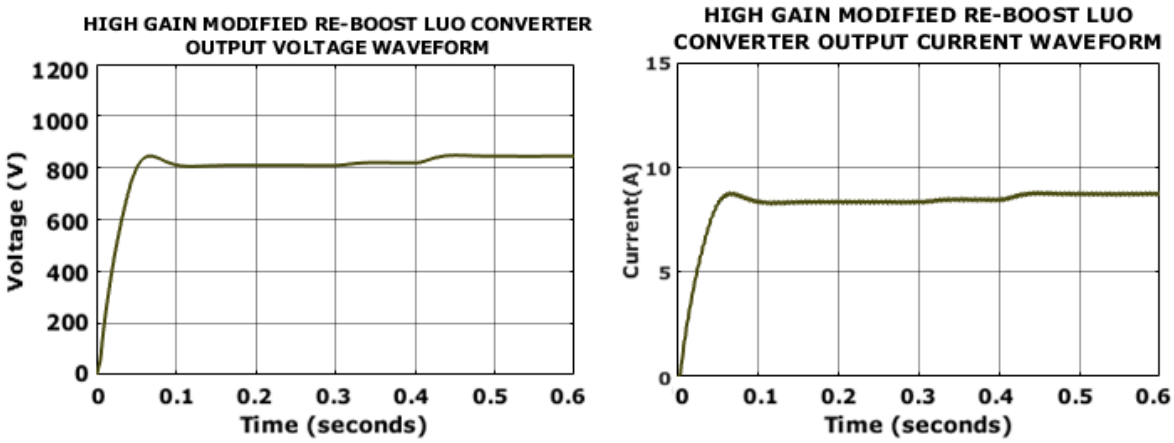

Fig. 12. Converter output (a) Voltage (b) Current.

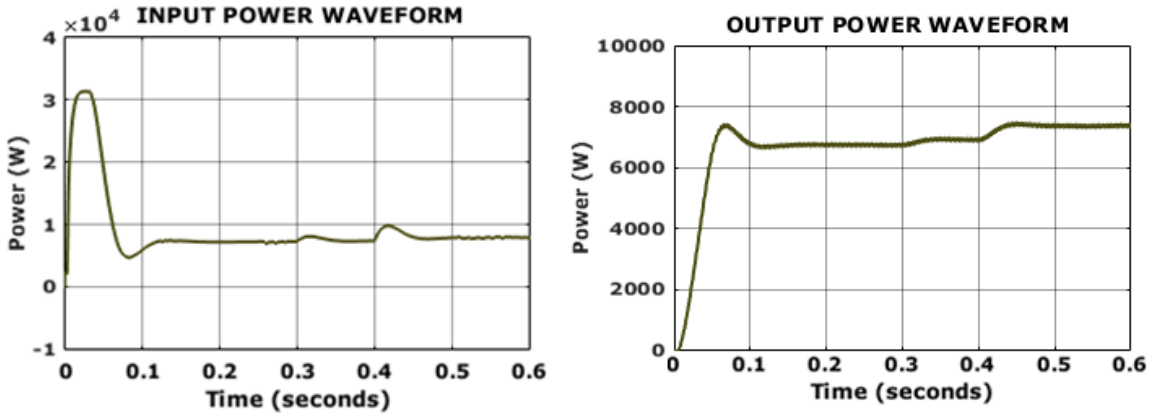

Fig. 13. Waveforms of input and output power.

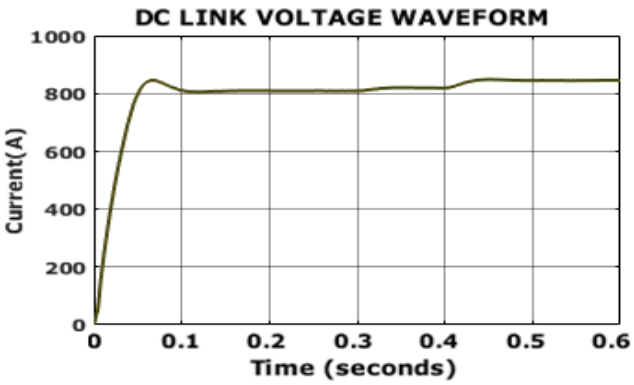

Fig. 14. Efficiency and DC link voltage waveform.

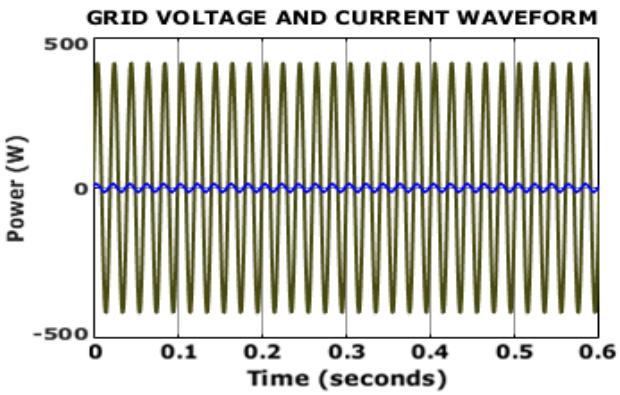

Fig. 16. Grid in-phase waveform.

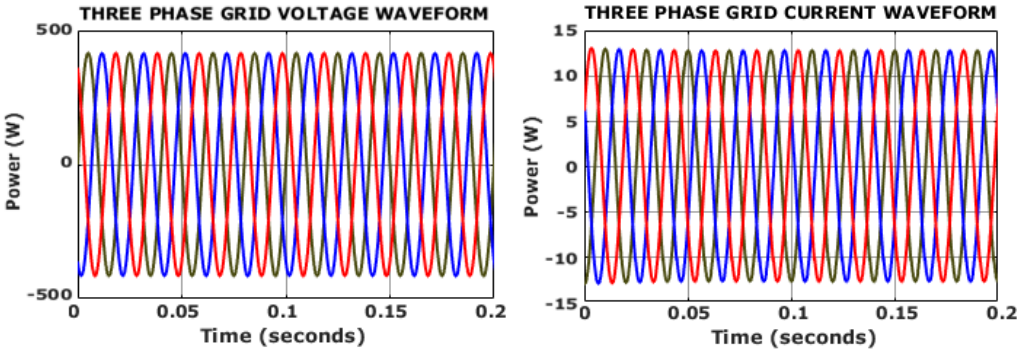

Fig. 15. Grid output Voltage and Current.

before abruptly declining to $800W$. This illustrates converter controls and maximizes energy output from PV source. Output power slightly increased to 7000W, indicating that the system is adapting occasionally. Converter's ability to preserve a steady output in spite of variations in input power is demonstrated when the output power finally stabilizes at $9800W$. The initial fluctuations are due to the system adapting its control parameters to suppress transients and regulate output.

DC link voltage waveform in Fig. 14 demonstrates that voltage changes over time. It is seen that, with respect to input, the proposed converter shows a boosted voltage. After a brief transient period, the waveform stabilizes, signifying that the voltage has attained its steady-state value of approximately 800–900 V.

Fig. 15 visualizes output behaviour of grid systems, it is noticed that grid voltage is stabilized at 415V, with current observed to be maintained at 12A, without any distortions. This balance ensures efficient and uniform power distribution across the phases.

The grid in-phase waveform with output voltage of 415V and current of 12A is displayed in Fig. 16. This ensures stability of the system, demonstrating smoother operation without any distortion, resulting in improved quality of power.

Real and reactive power waveforms are displayed in Fig. 17, where the real power is noticed to be consistent, maintaining at 9. The magnitude of the real power is $9.9\times10^{4}W$ over the period of time. Whereas the reactive power is observed to be stable, sustaining at 660VAR, illustrating the effectiveness of the system in handling reactive power components for grid integration.

Fig.18 portrays the Total Harmonic Distortion (THD) values for R, Y, and B phase, indicates that the proposed system results in reduced THD of 0.63%, 1.19%, and 1.17% for all three phases. By maintaining a lower THD, the system ensures that connected loads are supplied with steady and dependable electricity. Higher efficiency, longer equipment life, and fewer interruptions are all results of lower harmonics.

Table 2 shows comparative profile of converter topologies in terms of component count and efficiency. Proposed converter has better performance with an efficiency of 94.31% but with only six components a much lower number than for other designs. For instance, the Dual-Lift Hybrid Luo

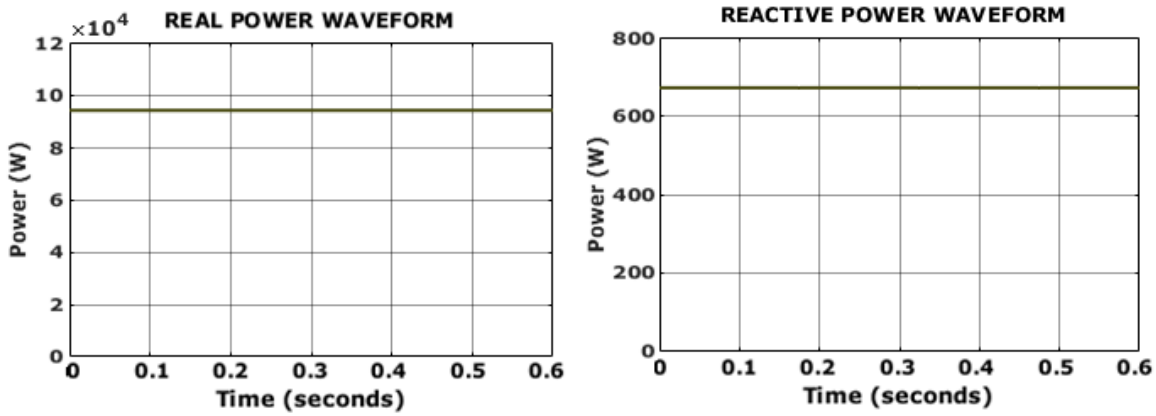

Fig. 17. Power waveform (a) Real (b) Reactive.

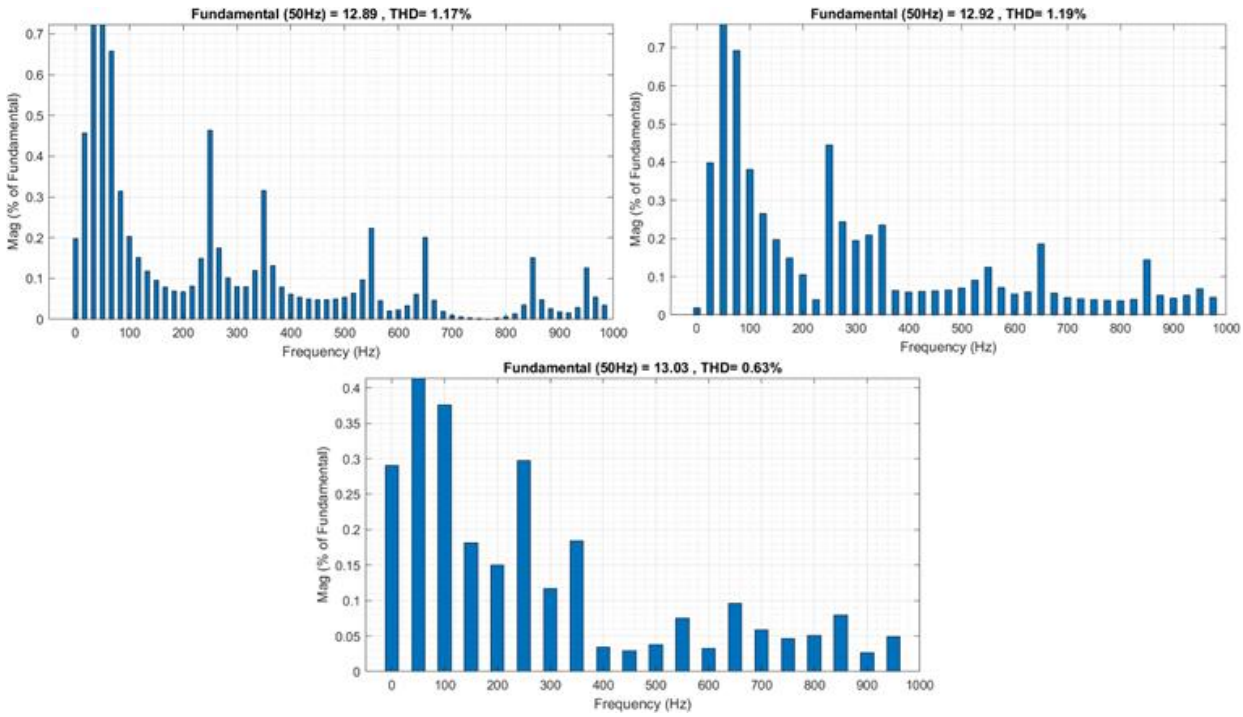

Fig. 18. THD waveform.

Converter [18] has an efficiency of 94% with ten components, whereas the Boost Integrated Luo Converter [17] has an efficiency of 92% with nine components. The Interleaved Luo Converter [16] with its use of eleven components provides an efficiency of only 90%. These findings highlight the optimized structure of the proposed converter, which operates to achieve maximum efficiency and a low number of components, thus being appropriate for energy-conscious and compact applications.

Fig. 19 shows the simulated conversion efficiency of the HG-MRBL stage with JSA-ANFIS MPPT and optimized PI control as a function of output load from 0 % to 100 % of nominal power. As load increases, the converter settles into its optimal soft-switching regime minimizing both conduction and switching losses. This yields a peak efficiency of 94.31 % at around nominal load, highlights the converter's robustness and its suitability for solar-to-grid applications.

Fig. 20 displays the MPPT tracking efficiencies of various algorithms implemented with the HG-MRBL converter. The earliest method by Zhuoli Zhao et al. (2021) yields the lowest efficiency at 92.77 %. Efrain Mendez et al. (2020) improve this to 96.25 %, followed by Asnad A. H. AlZubaidi et al.

Table 2. Analysis of converter Efficiency with existing

Converter Reference	Switches	Diodes	Capacitor	Inductor	Total No.of components	Efficiency (%)
Interleaved Luo Converter [16]	2	2	5	4	11	90%
Dual-Lift Hybrid Luo Converters [18]	2	4	2	4	10	94%
Boost Integrated Luo Converter [17]	1	2	3	3	9	92%
Proposed Converter	1	1	3	1	6	94.31

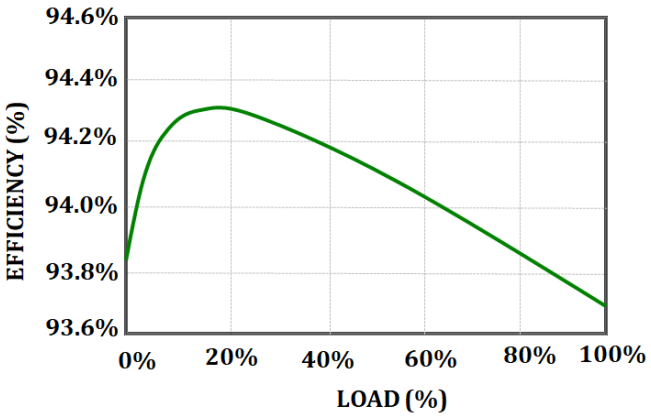

Fig. 19. Efficiency Curve of Proposed HG-MRBL converter.

(2022) at 97.02 % and Akhil Raj et al. (2022) at 97.86 %. Catalina González-Castano et al. (2021) achieve 98.92 %, and proposed JSA-ANFIS MPPT method tops the chart at 98.95 %. This steady rise from 92.77 % to 98.95 % reflects the incremental advances in algorithm design, culminating in our approach's marginal yet meaningful gain in extracting maximum power under varying PV conditions.

Fig. 21 compares the convergence performance of three MPPT techniques: JSA-ANFIS, ANFIS, and ANN. The JSA-ANFIS MPPT method demonstrates the fastest convergence with improved performance and minimal oscillations. While ANFIS converges slower than ANFIS, and ANN has the slowest convergence.

The Mean Square Error (MSE) trends for the JSA-ANFIS, ANFIS, and ANN MPPT approaches are depicted in the graph in Fig. 22. It is observed that JSA-ANFIS exhibits a significant reduction in MSE, reaching optimal performance

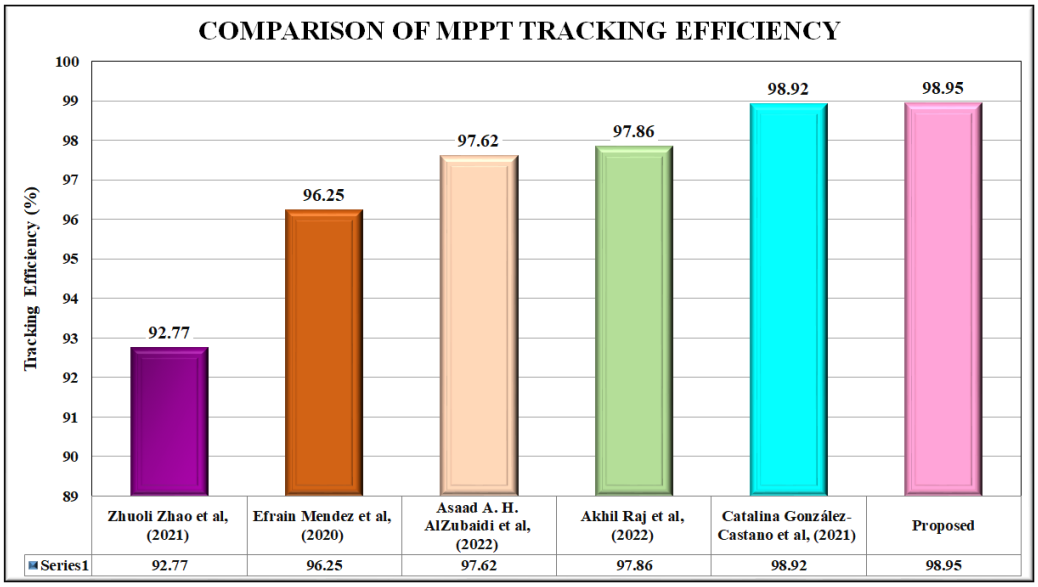

Fig. 20. Comparison of tracking efficiency.

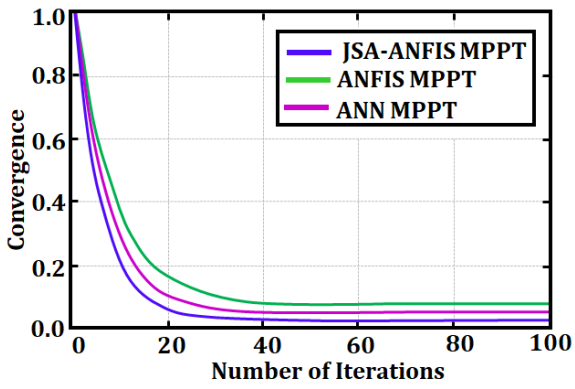

Fig. 21. Comparative Analysis of Convergence Characteristics.

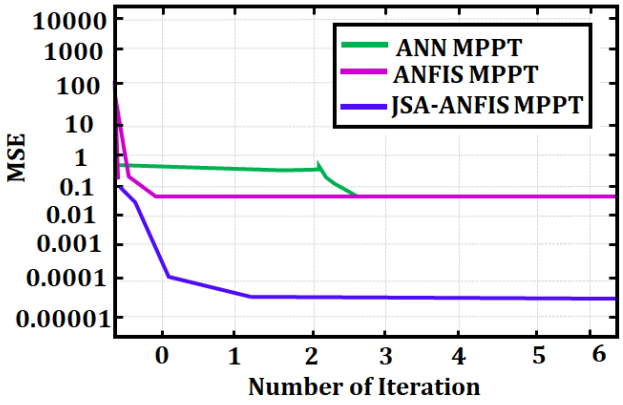

Fig. 22. Comparison of MSE.

with the fewest iterations. On the other hand, ANN exhibits larger MSE values and slower convergence, while the ANFIS follows with a steady but slower error reduction. The outcomes validate JSA-ANFIS's superiority in attaining accurate MPPT.

5- Conclusion

This research introduces an advanced solution for integrating PV systems with the grid, addressing key challenges in renewable energy applications. The development of an HG-MRBL converter coupled with a JSA-ANFIS for MPPT significantly enhances efficiency and reliability of a PV grid-tied system. Simulation results validate system's superior performance, achieving a converter efficiency of 94.31%, surpassing existing methods. The JSA-ANFIS MPPT demonstrates exceptional tracking efficiency, contributing to optimal energy harvesting under varying environmental conditions. This innovative approach ensures voltage stability, minimizes harmonics, and provides seamless power supply integration to the grid. The proposed system demonstrates the potential for sustainable energy solutions, providing solution for improved effective employment of renewable resources in modern energy systems. Future research will discover reliability of this design for larger systems and consider its incorporation with extra RESs.

References

[1] I. Akhtar, S. Kirmani, and M. Jameel, "Reliability Assessment of Power System Considering the Impact of Renewable Energy Sources Integration into Grid with Advanced Intelligent Strategies", 2021 In IEEE Access, vol. 9, pp. 32485-32497.

[2] M. S. Alam, F. S. Al-Ismail, A. Salem, and M. A. Abido, "High-Level Penetration of Renewable Energy Sources Into Grid Utility: Challenges and Solutions", 2020 In IEEE Access, vol. 8, pp. 190277-190299.

[3] M. G. Marangalu, N. V. Kurdkandi, K. K. Monfared, I. Talebian, Y. Neyshabouri, and H. Vahedi, "A New High Step-Up SC-Based Grid-Tied Inverter with Limited Charging Spike for RES Applications", 2024 In IEEE Open Journal of Power Electronics, vol. 5, pp. 295-310.

[4] V. K. Goyal, and A. Shukla, "Isolated DC–DC Boost Converter for Wide Input Voltage Range and Wide Load Range Applications", 2021 IEEE Transactions on Industrial Electronics, 2020, vol. 68, no. 10, pp. 9527-9539.

[5] K. S. Kavin, P. Subha Karuvelam, M. Devesh Raj, and M. Sivasubramanian, "A Novel KSK Converter with Machine Learning MPPT for PV Applications", 2024 Electric Power Components and Systems, pp. 1-19.

[6] A. Alfares, B. Lehman, and M. Amirabadi, "A Ćuk-Based Modular DC–DC Converter for Medium Voltage Direct Current (MVDC) Applications", 2020 IEEE Open Journal of Power Electronics, vol.3, pp.560-573.

[7] A. Nandanwar, P. V. Harisyam, S. Ghotgalkar, and K. Basu, "Continuous Control Set Model Predictive Control of Tri-state Boost Converter", 2023 IEEE Energy Conversion Congress and Exposition (ECCE), Nashville, TN, USA, pp. 2699-2705.

[8] K. Nathan, S. Ghosh, Y. Siwakoti, and T. Long, "A new DC–DC converter for photovoltaic systems: Coupledinductors combined cuk-SEPIC converter", 2019 IEEE Transactions on Energy Conversion, vol. 34, no. 1, pp. 191– 201.

[9] L. Mamouri, T. Mesbahi, and V. Frick, "MPPT Technique with Improved FOCV Control Applied to a Full Active Rectifier for Low-Voltage Piezoelectric Energy Harvesting", 2024 in IEEE Transactions on Circuits and Systems II: Express Briefs, vol. 71, no. 2, pp. 532-536.

[10] C. Yanarates, Y. Wang, and Z. Zhou, "Unity Proportional Gain Resonant and Gain Scheduled Proportional (PR-P) Controller-Based Variable Perturbation Size Real-Time Adaptive Perturb and Observe (P&O) MPPT Algorithm for PV Systems", 2021 In IEEE Access, vol. 9, pp.

138468-138482.

[11] R. Sangrody, S. Taheri, A. M. Cretu, and E. Pouresmaeil, "An Improved PSO-Based MPPT Technique Using Stability and Steady State Analyses Under Partial Shading Conditions", 2024 In IEEE Transactions on Sustainable Energy, vol. 15, no. 1, pp. 136-145.

[12] Y. Zhang, "Neural Network Algorithm with Reinforcement Learning for Parameters Extraction of Photovoltaic Models", 2023 in IEEE Transactions on Neural Networks and Learning Systems, vol. 34, no. 6, pp. 2806-2816.

[13] M. N. Ali, K. Mahmoud, M. Lehtonen, and M. M. F. Darwish, "An Efficient Fuzzy-Logic Based Variable-Step Incremental Conductance MPPT Method for Grid-Connected PV Systems", 2021 In IEEE Access, vol. 9, pp. 26420-26430.

[14] S. A. Ibrahim, A. Nasr, and M. A. Enany, "Maximum Power Point Tracking Using ANFIS for a Reconfigurable PV-Based Battery Charger under Non-Uniform Operating Conditions", 2021 in IEEE Access, vol. 9, pp. 114457-114467.

[15] S. Javed, K. Ishaque, S. A. Siddique, and Z. Salam, "A Simple Yet Fully Adaptive PSO Algorithm for Global Peak Tracking of Photovoltaic Array Under Partial Shading Conditions", 2022 in IEEE Transactions on Industrial Electronics, vol. 69, no. 6, pp. 5922-5930.

[16] B. Singh, and R. Kushwaha, "Power factor preregulation in interleaved Luo converter-fed electric vehicle battery charger", 2021 IEEE Transactions on Industry Applications, vol. 57, no. 3, pp. 2870-2882.

[17] V. A. Vijayarangan, and S. Kaliyaperumal, "Design of Boost Integrated Luo Converter for Grid Tied EV Based Charging Station", 2023 International Journal of Electrical and Electronics Research, vol. 11, no. 4, pp. 1167-1175.

[18] K. Kumar, V. Lakshmi Devi, C. Dhanamjayulu, H. Kotb, and A. ELrashidi, "Evaluation and deployment of a unified MPPT controller for hybrid Luo converter in combined PV and wind energy systems", 2024 Scientific Reports, vol. 14, no. 1, pp. 3248.

[19] Z. Zhao, M. Zhang, Z. Zhang, Y. Wang, R. Cheng, J. Guo, P. Yang, C. S. Lai, P. Li, and L. L. Lai, "Hierarchical pigeon-inspired optimization-based MPPT method for photovoltaic systems under complex partial shading conditions", 2021 IEEE Transactions on Industrial Electronics, vol. 69, no. 10, pp. 10129-10143.

[20] E. Mendez, A. Ortiz, P. Ponce, I. Macias, D. Balderas, and A. Molina, "Improved MPPT algorithm for photovoltaic systems based on the earthquake optimization algorithm", 2020 Energies, vol. 13, no. 12, pp. 3047.

[21] A. A. H. AlZubaidi, L. A. Khaliq, H. S. Hamad, W. K. Al-Azzawi, M. S. Jabbar, and T. A. Shihab, "MPPT implementation and simulation using developed P&O algorithm for photovoltaic system concerning efficiency", 2022 Bulletin of Electrical Engineering and Informatics, vol. 11, no. 5, pp. 2460-2470.

[22] A. Raj, and R. P. Praveen, "Highly efficient DC-DC boost converter implemented with improved MPPT algorithm for utility level photovoltaic applications", 2022 Ain Shams Engineering Journal, vol. 13, no. 3, pp.101617.

[23] C. González-Castaño, C. Restrepo, S. Kouro, and J. Rodriguez, "MPPT algorithm based on artificial bee colony for PV system", 2021 IEEE Access, vol. 9, pp. 43121-43133.

HOW TO CITE THIS ARTICLE

K. Sravani, Ch. Leela Kumari, P. Manisha, R. Sowmya Deepika, Y. Manoj, High Gain Modified Reboost-Luo Converter with Optimized PI Controller for Effectual Integration of PV in Grid System, AUT J. Elec. Eng., 58(2) (2026) 247-262.

DOI: 10.22060/eej.2026.24345.5687